Edge-State Wave Functions from Momentum-Conserving Tunneling Spectroscopy

T. Patlatiuk,[1] C. P. Scheller,[1] D. Hill,[2] Y. Tserkovnyak,[2] J. C. Egues,[3] G. Barak,[4] A. Yacoby,[4] L. N. Pfeiffer,[5] K. W. West,[5] and D. M. Zumbühl[1,*]

[1]*Departement Physik, University of Basel, Klingelbergstrasse 82, CH-4056 Basel, Switzerland*
[2]*Department of Physics and Astronomy, University of California, Los Angeles, California 90095, USA*
[3]*Instituto de Física de São Carlos, Universidade de São Paulo, 13560-970 São Carlos, São Paulo, Brazil*
[4]*Department of Physics, Harvard University, Cambridge, Massachusetts 02138, USA*
[5]*Department of Electrical Engineering, Princeton University, Princeton, New Jersey 08544, USA*

(Received 12 February 2020; accepted 21 July 2020; published 21 August 2020)

We perform momentum-conserving tunneling spectroscopy using a GaAs cleaved-edge overgrowth quantum wire to investigate adjacent quantum Hall edge states. We use the lowest five wire modes with their distinct wave functions to probe each edge state and apply magnetic fields to modify the wave functions and their overlap. This reveals an intricate and rich tunneling conductance fan structure which is succinctly different for each of the wire modes. We self-consistently solve the Poisson-Schrödinger equations to simulate the spectroscopy, reproducing the striking fans in great detail, thus, confirming the calculations. Further, the model predicts hybridization between wire states and Landau levels, which is also confirmed experimentally. This establishes momentum-conserving tunneling spectroscopy as a powerful technique to probe edge state wave functions.

DOI: 10.1103/PhysRevLett.125.087701

Edge states play a key role in materials with a nontrivial topology establishing a conducting boundary around a (nominally) insulating bulk in novel topological insulators as well as quantum (spin) Hall materials [1–8]. Despite clear theoretical understanding, only a few experiments could probe and resolve edge states in systems with steep, hard wall-like confinement potentials [9–17]. In semiconductor heterostructures with typical gate defined or etched structures, strong confinement is difficult to produce, opening the door for Coulomb interactions to dominate and leading, e.g., to issues like edge state reconstruction [18,19]. On the other hand, steep confinement can arise naturally by virtue of the sample fabrication, for example, in van der Waals heterostructures [20] or in GaAs quantum wells cleaved and overgrown *in situ* in a molecular beam epitaxy chamber (cleaved edge overgrowth) [9–17].

The wave function profiles of edge states are very difficult to access in experiments, and their properties are often inferred from standard transport measurements [21–23], which may also suffer from remnant bulk conductivity [24]. Scanning probe techniques can offer valuable additional insight into localized states [25,26] as well as edge states both in quantum Hall (QH) [27–30] and in quantum spin Hall [24,31–33] regimes. However, scanning probe methods also have a number of limitations including poor resolution and invasive probes. Thus, establishing methods to directly access the edge state wave function is a great challenge.

In this Letter, we use tunneling into modes of a cleaved-edge overgrowth quantum wire as an energy and

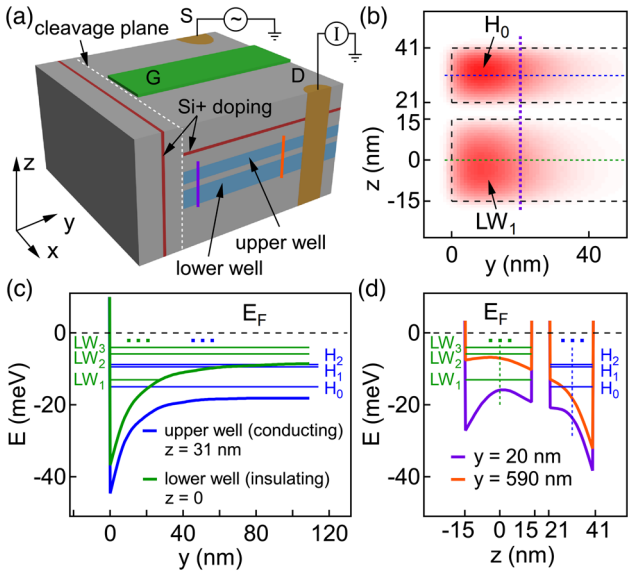

FIG. 1. (a) Sample schematic (not to scale) with upper and lower quantum well (light blue) together with top and side Si dopants (red). A surface gate G (green) of 2 μm width controls the local electron density. Source and drain ohmic contacts (brown) are labeled S and D, respectively. (b) Wave function $\psi(y,z)$ for the ground state H_0 (LW_1) in the upper (lower) quantum well. Dashed lines indicate locations of cuts shown in (c) and (d). (c) Conduction band profiles along the y direction in the upper (blue) and lower (green) quantum wells. Horizontal lines represent the lowest three eigenenergies. (d) Conduction band profile along the z direction 20 nm (purple) and 590 nm (orange) away from the cleavage plane [dashed white in (a)].

momentum selective spectrometer to investigate the wave functions of QH edge states in an adjacent quantum well, see sample schematic in Fig. 1(a). We measure the resonant tunneling conductance, related to the wave function overlap, as a function of in-plane magnetic field B_Y, which controls the relative momentum, and perpendicular magnetic field B_Z, which predominantly modifies the QH wave functions. This produces a set of fans of intricately growing and fading curves, see Fig. 2. We self-consistently simulate the edge state and quantum wire wave functions, see Figs. 1(b) and 3, which allows us to calculate the measured tunneling conductance. We find very good agreement with experiment, thus, confirming the validity of the calculated wave functions.

The schematic cross section of the double quantum well sample used in this study is shown in Fig. 1(a). It contains upper and lower GaAs quantum wells (blue) separated by a thin AlGaAs tunnel barrier (gray). A doping layer (red) above the upper well provides charges for a high-mobility upper two-dimensional electron gas (2DEG), while electron density in the lower well is below the conduction threshold, making it insulating, as if there was no lower 2DEG. Dopants deposited above an *in situ* cleaved surface [10] (vertical red) create a quasitriangular confinement potential forming extended 1D wire modes in both upper and lower wells. We name these modes $\mathrm{LW}_1, \mathrm{LW}_2, \ldots$ in the lower wire (LW). In the upper system, the 1D wire modes hybridize with the Landau levels present at finite B_Z and form what we refer to as hybrid states $H_0, H_1, \ldots$. In this double quantum well sample, momentum selective spectroscopy allows us to use the lower wire modes $\mathrm{LW}_{1,2,\ldots}$ to probe the upper system hybrid states $H_{0,1,\ldots}$.

Source and drain ohmic contacts are attached far away from the cleavage plane, see Ref. [17] for further sample details. Electrical conductance between the source (S) and drain (D) was measured as a function of magnetic field $\mathbf{B} = (B_Y, B_Z)$, orientations are shown in Fig. 1(a). To tune the double well device into the tunneling regime, a negative voltage was applied to the surface gate G (green) locally depleting all the states in the upper quantum well. In this configuration, electrons propagate from source through the 2DEG into the hybrid states, then tunnel to the lower wire, propagate along the lower wire under the gate, and finally tunnel back into the upper well. See [34] for measurement details.

Because of translational invariance in the tunneling region away from the gate, electron momentum k_x is conserved during the tunneling between the upper and lower systems, giving resonant tunneling when states in the upper and lower system have matching momenta. The in-plane magnetic field B_Y changes the electron momenta by $\Delta k_x = e d_Z B_Y/\hbar$, where d_Z is the z displacement between the center of mass of initial and final states. Similarly, the perpendicular magnetic field B_Z provides another

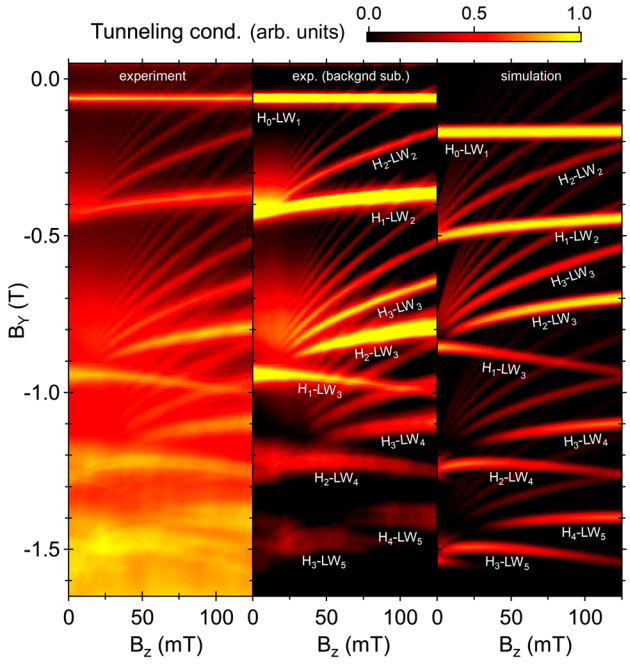

FIG. 2. Experimental (left and middle) and theoretical (right) tunneling conductance between various hybrid states and lower wire modes as a function of out-of-plane (B_Z) and in-plane (B_Y) magnetic fields. For the middle panel, a smooth background is subtracted from the experimental data and an oversaturated color scale is used to emphasize weak features. The tunneling conductance to the lower wire mode LW_2 is strongest for the hybrid state H_1 and depends weakly on the magnetic field B_Z. In contrast, the tunneling conductance to the wire modes $\mathrm{LW}_{3,4,5}$ shows significant strength variations as magnetic field B_Z is increased, see main text for details.

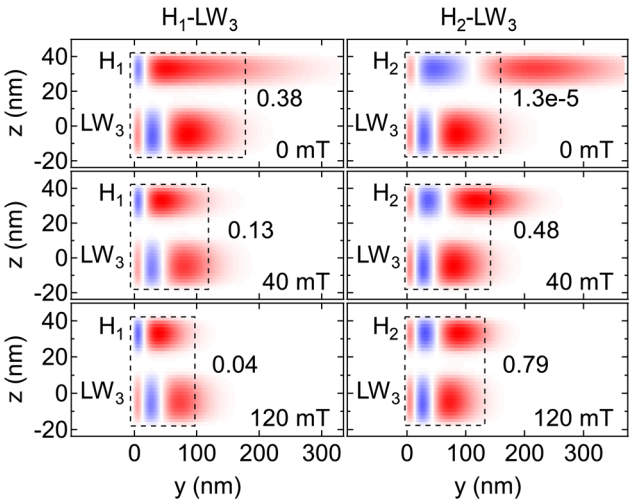

FIG. 3. Evolution of the wave functions of the hybrid state H_1 (left column), H_2 (right column), and lower wire mode (LW_3) as a function of magnetic field B_Z. The cleaved edge is at $y = 0$. The squared overlap normalized to its maximal value in Fig. 2 is indicated in each panel. Red and blue colors represent the signs of the probability amplitude.

contribution to the momentum shift $\Delta k_x = e d_Y B_Z/\hbar$ for states displaced by d_Y in the y direction and, also, sets the Landau level energies.

The resulting spectroscopy using both magnetic fields B_Y and B_Z displays several intricate fan structures of rising and decreasing curves, as shown in Fig. 2. Each fan arises from tunneling to one of the lower wire modes $\mathrm{LW}_2, \mathrm{LW}_3, \ldots$. The fans appear at increasingly more negative B_Y corresponding to the Fermi momenta of the lower wire modes. Each curve within a fan corresponds to a hybrid state (upper system). The labeling of curves is obtained from a careful analysis from a larger B-field scan (shown in Ref. [17]). The left panel of Fig. 2 displays the measured differential conductance with magnetic fields rotated into the sample coordinate system (details in [34]). On the middle panel, a smooth background was subtracted to emphasize the peak structure. The right panel shows the simulated results.

The horizontal line close to $B_Y = 0$ corresponds to tunneling between the lowest modes in the upper (H_0) and lower (LW_1) systems. The top most fan originates from tunneling into LW_2, shows the strongest signal for tunneling from the state H_1 and weaker tunneling for the states with higher orbital indices ($H_2, H_3 \ldots$). The second fan results from the tunneling into LW_3, shows substantial decrease of the tunneling signal for H_1 as the magnetic field B_Z increases and opposite behavior for H_2. The other curves of this fan have a maximum at intermediate values of B_Z accompanied by small signal at low and high fields. The fan originating from tunneling into LW_4 is very similar to the fan LW_3 with the difference that the indices of all the curves of this fan are shifted up by one and the first curve disappears completely already at small fields. Similar behavior is observed for the fan with tunneling into LW_5, showing a decreasing signal for H_3 and an increasing signal H_4, and again, very strong suppression of the lower states, here, H_0, H_1, and H_2.

To explain this rich and striking pattern of the tunneling conductance, we have numerically calculated the wave functions for the states in the upper and lower systems using a 2D self-consistent Schrödinger-Poisson solver [38]. The wave function of an electron is written as a product of a plane wave with momenta k_x and the self-consistent solutions in y-z plane

$$\Psi^j_{n,k_x}(x,y,z) = e^{ik_x x}\psi^j_n(y,z). \tag{1}$$

The index n enumerates different orbital states, $j = u$ denotes the upper system, and $j = l$ the lower system. Figure 1(b) shows the $\psi^u_0(y,z)$ and $\psi^l_1(y,z)$ components of the wave functions H_0 and LW_1. The conduction band along the y and z directions are shown in Figs. 1(c) and 1(d), respectively. A decrease of the conduction band energy close to the cleavage plane at $y = 0$ is caused by the electric field of the overgrown ionized dopants nearby at $y < 0$. The resulting triangular confinement potential in Fig. 1(c) leads to the presence of several lower wire modes. The energy of the state H_0 is above the conduction band in the bulk of the sample, see Fig. 1(c), while having significant weight only close to the cleavage plane, Fig. 1(b). The small energy and Fermi momentum difference between the states H_1 and H_2 (and higher states H_i) are consistent with the appearance of the corresponding resonances at almost the same B_Y field at $B_Z = 0$, see Fig. 2.

The Landau gauge $\mathbf{A} = (zB_Y - yB_Z, 0, 0)$ was used to describe the system at finite magnetic field $\mathbf{B}$, as it captures the translational invariance along the x direction. In this gauge, momentum k_x is a good quantum number, so the total wave function $\Psi^j_{n,k_x}(x,y,z,B)$ can be written analogously to Eq. (1). Here, ψ^j_n was calculated under the assumption that, at a finite magnetic field, the Fermi level and electrostatic confinement potential are the same as at $\mathbf{B} = 0$. This assumption is justified as small magnetic fields do not modify the electron density much.

Using Fermi's golden rule, the tunneling conductance between state H_n in the upper and state LW_m in the lower systems can be written as

$$G_{n\to m} = \frac{2\pi e}{\hbar} t^2 \rho_u \rho_l \lambda^2_{n\to m}, \tag{2}$$

where e is electron charge, $\hbar$ is the Plank constant, t is the tunneling coupling strength, ρ_j is the density of states, and $\lambda_{n\to m}$ is the wave function overlap between the ψ^u_n and ψ^l_m states. An additional series resistance due to the lower wire under the gate was included. The calculated tunneling conductance into lower wire modes $\mathrm{LW}_1 - \mathrm{LW}_5$ is displayed in the right panel of Fig. 2, giving excellent agreement to the experiment. The observed conductance evolution can be explained by a simple selection rule. If the number of wave-function lobes in the tunneling region is the same for the initial and final states, then the conductance is strong. Otherwise, it is weak due to near orthogonality. The tunneling region is defined as the region in space where the wave functions in the upper and lower systems have a significant overlap (see Supplemental Material [34]).

As an example, we will focus on the $H_2 - \mathrm{LW}_3$ resonance. The simulated wave functions of states H_2 and LW_3 at $B_Z = 0$ are shown in the top right panel of Fig. 3. The tunneling region, shown as a dashed box, is limited by the smaller wave function, in this case LW_3. For these two states, the number of lobes in the tunneling box at zero field differs by one, resulting in small overlap and correspondingly low tunneling conductance. This is consistent with the measured small conductance of the $H_2 - \mathrm{LW}_3$ resonance at small B_Z field in Fig. 2. As the magnetic field is increased (Fig. 3 lower right panels) the already electrostatically more confined wire state LW_3 is hardly affected while the more spread out hybrid state H_2

is compressed, and thus, the third lobe starts to enter the tunneling region. Thus, the overlap between the wave functions grows with field, consistent with the observed increase in tunneling conductance for this resonance in both simulation and experiment in Fig. 2. An exception from this rule occurs when the overlap is dominated by the contribution from the outermost lobes of the wave functions, the case for the resonance $H_1 - \mathrm{LW}_3$ at $B_Z = 0$, shown in the top left panel of Fig. 3, see [34] for details.

The amount of top and side dopants in the structure strongly affects the B_Y position of the resonances, and here, we adjusted both doping levels to match the positions of the simulated $H_n - \mathrm{LW}_2$ and $H_n - \mathrm{LW}_3$ resonances with experiment. Only the resonances $H_n - \mathrm{LW}_4$ and $H_n - \mathrm{LW}_5$ were slightly shifted down by hand in Fig. 2 to agree with experiment. We note that the doping levels do not qualitatively affect the tunneling strength and the B_Z dependence. The excellent agreement between the single particle theory and experiment covering numerous distinct and complicated features, see Fig. 2, is a very strong indication of the validity of the calculated wave functions.

The triangular potential from the ionized overgrowth donors combined with the parabolic magnetic field confinement leads to a k_x-momentum dependent hybridization of the wire and quantum Hall states in the upper systems, shown in Figs. 4(a) and 4(b). We note that k_x is linked to the guiding center position y_0 of the parabolic magnetic confinement via $y_0 = k_x l_B^2$, with magnetic length $l_B = \sqrt{\hbar/eB_Z}$. Going through the k_x axis, three distinct regimes separated by two anticrossings can be distinguished for each hybrid state (except for H_0, which undergoes only one anticrossing). Here, we pick the hybrid state H_1 as an example, with dispersion shown in Fig. 4(a) and wave functions in Fig. 4(b), both in dashed orange. This hybrid state behaves as a wire mode between the two anticrossings and as a Landau level everywhere else, including states close to the Fermi level that are involved in the tunneling.

First, far away from the edge, corresponding to large k_x momentum (square markers), this state has essentially the wave function of the second Landau level in the bulk. As k_x is lowered, the state anticrosses with the hybrid state H_2 (stars), where the wave function hybridizes and delocalizes over the two minima in the potential (blue). The state H_2 in this anticrossing is the antibonding state with antisymmetric combination, shown in solid orange, featuring one additional node.

Second, for a small range of momenta k_x, the wave function of the state H_1 resembles that of the lowest wire mode (triangles), though still with one node and a very small negative amplitude in the parabolic minimum (shown amplified, here, for clarity). For even smaller momenta, the state undergoes a second hybridization (cross), now with hybrid state H_0 (red). In a similar way, the upper wire mode hybridizes with all Landau levels, weaving through numerous anticrossings, which, together, are forming the parabolic wire dispersion at positive momenta, as seen in Fig. 4(a). At each anticrossing, the wave function acquires one additional node when moving up one state in energy.

Third, and finally, for negative k_x (circle), the wave function is pushed more against the wall and more strongly confined by the magnetic field, thus, increasing the energies of the states [Fig. 4(a)], still exhibiting one node, similar to the second wire mode but with magnetic field.

The density at the cleaved edge is higher than in bulk due to the wire mode, see [34]. Signatures of the hybridization, as discussed above, are present in the tunneling conductance, see Fig. 5, shown over a wider range of magnetic field B_Z compared to Fig. 2. Insets qualitatively depict the dispersion relations of the hybrid states (red) and LW_1

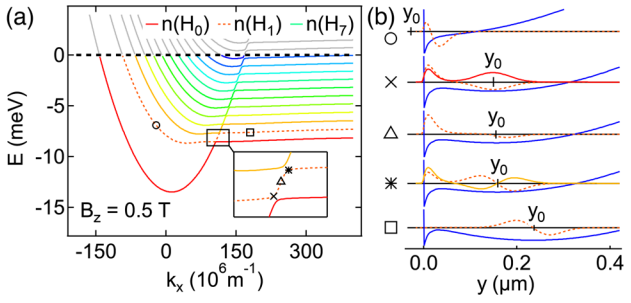

FIG. 4. (a) Dispersion of hybrid states ($H_0, H_1, \ldots$, colors) in the upper system. Empty states above the Fermi level are shown in gray. (b) The wave function of the hybrid state H_0 (red), H_1 (dashed orange), H_2 (solid orange), and the total electrostatic confinement potential (blue) at $z = 31$ nm in the upper system for a range of values of the guiding center position y_0. The corresponding momenta k_x are indicated with markers in (a).

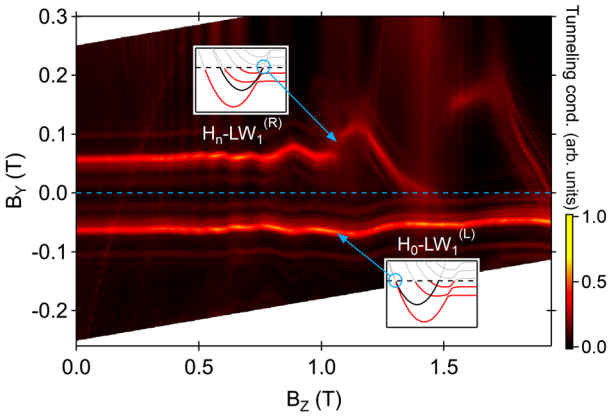

FIG. 5. Tunneling conductance between hybrid states in the upper system and the lower wire mode LW_1. Insets qualitatively depict the dispersion relation of the hybrid states (red) and LW_1 (black) for B_Y and B_Z which satisfy the resonant tunneling condition. Measurements extended for $B_Z < 0$ are shown in Fig. S10 in the Supplemental Material [34].

mode (black) for the resonances indicated by the arrows. The resonance at negative B_Y originates from the tunneling into the states close to the left Fermi point of the lower wire $\mathrm{LW}_1^{(L)}$ (blue circle, lower inset). This resonance remains mostly unchanged in B_Y as the magnetic field B_Z is increased, giving a nearly horizontal feature as long as the wire confinement is dominant (for the full B_Z range of Fig. 5). In contrast, the resonance originating from the right Fermi point $\mathrm{LW}_1^{(R)}$, tracks the anticrossings of the hybrid states (blue circle, upper inset), leading to strong motion in B_Y. As the magnetic field B_Z is increased, the topmost hybrid state is moving through the Fermi level, going through the regimes described in Fig. 4(b). This results even in some discontinuities when an avoided crossing is passing the Fermi level and the momentum is jumping to large k_x to the next lower hybrid, as seen in Fig. 5.

In summary, we measured the tunneling conductance between the QH edge states and the lower wire mode as a function of both in-plane and out-of-plane magnetic fields. We show that the tunneling conductance calculated using numerically simulated wave functions reproduces the intricate fan structures with numerous striking features observed in experiment, giving a strong indication of the validity of the simulated wave functions. We formulate a simple selection rule to estimate the resonance strength based on wave function overlap or orthogonality in the tunneling region. The simulation also provides the dispersions exhibiting hybridization between the wire mode and the Landau levels with numerous anticrossings. Indeed, upon inspection of the corresponding magnetic field range, we observe the predicted jumps of the resonances due to the anticrossings, thus, providing further confirmation of the simulation.

The method used in this study could also be applied to probe spin split edge states or fractional QH edge states, e.g., with filling factors $\nu = 4/3$ or $5/3$, which are, in fact, observed in this device. Additionally, samples with a side gate could be used to directly study influence of the confinement potential on the wave function of the QH edge and wire states. Finally, similar tunneling spectroscopy from a 1D conductor such as a nanowire or nanotube could also be used to probe edge states of topological insulators or other edge state materials of interest.

The data that support the findings of this study are available in a Zenodo repository [39].

This work was supported by the Swiss Nanoscience Institute (SNI), NCCR QSIT, Swiss NSF Grant No. 179024, ERC Starting Grant (DMZ), the EU H2020 European Microkelvin Platform EMP, Grant No. 824109, Brazilian Grants No. 2016/08468-0 and No. 2016/50200-4 (SPRINT program), both Sao Paulo Research Foundation (FAPESP), and Grant No. 306122/2018-9 from Conselho Nacional de Pesquisas (CNPq). The work at UCLA was supported by NSF Grant No. DMR-1742928.

T. P. and C. P. S. contributed equally to this work.

*dominik.zumbuhl@unibas.ch

[1] D. C. Tsui, H. L. Stormer, and A. C. Gossard, Phys. Rev. Lett. **48**, 1559 (1982).
[2] H. L. Stormer, Z. Schlesinger, A. Chang, D. C. Tsui, A. C. Gossard, and W. Wiegmann, Phys. Rev. Lett. **51**, 126 (1983).
[3] E. E. Mendez, W. I. Wang, L. L. Chang, and L. Esaki, Phys. Rev. B **30**, 1087 (1984).
[4] K. S. Novoselov, A. K. Geim, S. V. Morozov, D. Jiang, M. I. Katsnelson, I. V. Grigorieva, S. V. Dubonos, and A. A. Firsov, Nature (London) **438**, 197 (2005).
[5] Y. Zhang, Y. Tan, H. L. Stormer, and P. Kim, Nature (London) **438**, 201 (2005).
[6] M. Konig, S. Wiedmann, C. Brune, A. Roth, H. Buhmann, L. W. Molenkamp, X.-L. Qi, and S.-C. Zhang, Science **318**, 766 (2007).
[7] A. Tsukazaki, A. Ohtomo, T. Kita, Y. Ohno, H. Ohno, and M. Kawasaki, Science **315**, 1388 (2007).
[8] A. Tsukazaki, S. Akasaka, K. Nakahara, Y. Ohno, H. Ohno, D. Maryenko, A. Ohtomo, and M. Kawasaki, Nat. Mater. **9**, 889 (2010).
[9] L. N. Pfeiffer, K. W. West, H. L. Störmer, J. P. Eisenstein, K. W. Baldwin, D. Gershoni, and J. Spector, Appl. Phys. Lett. **56**, 1697 (1990).
[10] A. Yacoby, H. L. Störmer, N. S. Wingreen, L. N. Pfeiffer, K. W. Baldwin, and K. W. West, Phys. Rev. Lett. **77**, 4612 (1996).
[11] A. Yacoby, H. L. Störmer, K. W. Baldwin, L. N. Pfeiffer, and K. W. West, Solid State Commun. **101**, 77 (1997).
[12] O. M. Auslaender, A. Yacoby, R. de Picciotto, K. W. Baldwin, L. N. Pfeiffer, and K. W. West, Science **295**, 825 (2002).
[13] W. Kang, H. L. Stormer, L. N. Pfeiffer, K. W. Baldwin, and K. W. West, Nature (London) **403**, 59 (2000).
[14] M. Huber, M. Grayson, M. Rother, W. Biberacher, W. Wegscheider, and G. Abstreiter, Phys. Rev. Lett. **94**, 016805 (2005).
[15] M. Grayson, L. Steinke, D. Schuh, M. Bichler, L. Hoeppel, J. Smet, K. v. Klitzing, D. K. Maude, and G. Abstreiter, Phys. Rev. B **76**, 201304(R) (2007).
[16] L. Steinke, P. Cantwell, E. Stach, D. Schuh, A. Fontcuberta i Morral, M. Bichler, G. Abstreiter, and M. Grayson, Phys. Rev. B **87**, 165428 (2013).
[17] T. Patlatiuk, C. P. Scheller, D. Hill, Y. Tserkovnyak, G. Barak, A. Yacoby, L. N. Pfeiffer, K. W. West, and D. M. Zumbühl, Nat. Commun. **9**, 3692 (2018).
[18] D. B. Chklovskii, B. I. Shklovskii, and L. I. Glazman, Phys. Rev. B **46**, 4026 (1992).
[19] C. de C. Chamon and X. G. Wen, Phys. Rev. B **49**, 8227 (1994).
[20] G. Li, A. Luican-Mayer, D. Abanin, L. Levitov, and E. Y. Andrei, Nat. Commun. **4**, 1744 (2013).

[21] B. W. Alphenaar, P. L. McEuen, R. G. Wheeler, and R. N. Sacks, Phys. Rev. Lett. **64**, 677 (1990).
[22] A. Roth, C. Brüne, H. Buhmann, L. W. Molenkamp, J. Maciejko, X.-L. Qi, and S.-C. Zhang, Science **325**, 294 (2009).
[23] C. Brüne, A. Roth, E. G. Novik, M. König, H. Buhmann, E. M. Hankiewicz, W. Hanke, J. Sinova, and L. W. Molenkamp, Nat. Phys. **6**, 448 (2010).
[24] M. König, M. Baenninger, A. G. F. Garcia, N. Harjee, B. L. Pruitt, C. Ames, P. Leubner, C. Brüne, H. Buhmann, L. W. Molenkamp, and D. Goldhaber-Gordon, Phys. Rev. X **3**, 021003 (2013).
[25] S. H. Tessmer, P. I. Glicofridis, R. C. Ashoori, L. S. Levitov, and M. R. Melloch, Nature (London) **392**, 51 (1998).
[26] G. A. Steele, R. C. Ashoori, L. N. Pfeiffer, and K. W. West, Phys. Rev. Lett. **95**, 136804 (2005).
[27] A. Yacoby, T. A. Fulton, H. F. Hess, L. N. Pfeiffer, and K. W. West, Physica (Amsterdam) **20E**, 65 (2003).
[28] M. E. Suddards, A. Baumgartner, M. Henini, and C. J. Mellor, New J. Phys. **14**, 083015 (2012).
[29] K. Lai, W. Kundhikanjana, M. A. Kelly, Z.-X. Shen, J. Shabani, and M. Shayegan, Phys. Rev. Lett. **107**, 176809 (2011).
[30] N. Pascher, C. Rössler, T. Ihn, K. Ensslin, C. Reichl, and W. Wegscheider, Phys. Rev. X **4**, 011014 (2014).
[31] K. C. Nowack, E. M. Spanton, M. Baenninger, M. König, J. R. Kirtley, B. Kalisky, C. Ames, P. Leubner, C. Brüne, H. Buhmann, L. W. Molenkamp, D. Goldhaber-Gordon, and K. A. Moler, Nat. Mater. **12**, 787 (2013).
[32] E. Y. Ma, M. R. Calvo, J. Wang, B. Lian, M. Mühlbauer, C. Brüne, Y.-T. Cui, K. Lai, W. Kundhikanjana, Y. Yang, M. Baenninger, M. König, C. Ames, H. Buhmann, P. Leubner, L. W. Molenkamp, S.-C. Zhang, D. Goldhaber-Gordon, M. A. Kelly, and Z.-X. Shen, Nat. Commun. **6**, 7252 (2015).
[33] Y. Shi, J. Kahn, B. Niu, Z. Fei, B. Sun, X. Cai, B. A. Francisco, D. Wu, Z.-X. Shen, X. Xu, D. H. Cobden, and Y.-T. Cui, Sci. Adv. **5**, eaat8799 (2019).
[34] See Supplemental Material at http://link.aps.org/supplemental/10.1103/PhysRevLett.125.087701 for the details of the measurements, tunneling between states and its interpretation, exception to selection rule, hybridization, density profiles, and numerical calculations, which includes Refs. [35–37].
[35] C. P. Scheller, S. Heizmann, K. Bedner, D. Giss, M. Meschke, D. M. Zumbhl, J. D. Zimmerman, and A. C. Gossard, Appl. Phys. Lett. **104**, 211106 (2014).
[36] D. E. F. Biesinger, C. P. Scheller, B. Braunecker, J. Zimmerman, A. C. Gossard, and D. M. Zumbühl, Phys. Rev. Lett. **115**, 106804 (2015).
[37] D. Maradan, L. Casparis, T.-M. Liu, D. E. F. Biesinger, C. P. Scheller, D. M. Zumbühl, J. D. Zimmerman, and A. C. Gossard, J. Low Temp. Phys. **175**, 784 (2014).
[38] M. Rother, *2D Schrödinger Poisson solver* AQUILA, MATLAB *Central File Exchange* (Mathworks Inc., Natick, Massachusetts, 2009).
[39] T. Patlatiuk, C. P. Scheller, D. Hill, Y. Tserkovnyak, J. C. Egues, G. Barak, A. Yacoby, L. N. Pfeiffer, K. W. West, and D. M. Zumbuhl, Supporting data for edge-state wave functions from momentum-conserving tunneling spectroscopy, https://doi.org/10.5281/zenodo.3973330 (2020).